

REPORT

# Coordinated internodal and paranodal adhesion controls accurate myelination by oligodendrocytes

Nimrod Elazar<sup>1</sup>, Anya Vainshtein<sup>1</sup>, Katya Rechav<sup>2</sup> , Michael Tsoory<sup>3</sup>, Yael Eshed-Eisenbach<sup>1</sup>, and Elior Peles<sup>1</sup> 

**Oligodendrocyte–axon contact is mediated by several cell adhesion molecules (CAMs) that are positioned at distinct sites along the myelin unit, yet their role during myelination remains unclear. *Cadm4* and its axonal receptors, *Cadm2* and *Cadm3*, as well as myelin-associated glycoprotein (MAG), are enriched at the internodes below the compact myelin, whereas NF155, which binds the axonal Caspr/contactin complex, is located at the paranodal junction that is formed between the axon and the terminal loops of the myelin sheath. Here we report that *Cadm4*-, MAG-, and Caspr-mediated adhesion cooperate during myelin membrane ensheathment. Genetic deletion of either *Cadm4* and MAG or *Cadm4* and Caspr resulted in the formation of multimyelinated axons due to overgrowth of the myelin away from the axon and the forming paranodal junction. Consequently, these mice displayed paranodal loops either above or underneath compact myelin. Our results demonstrate that accurate placement of the myelin sheath by oligodendrocytes requires the coordinated action of internodal and paranodal CAMs.**

## Introduction

Myelin is a multilamellar membrane sheath produced by two types of glial cells: oligodendrocytes in the central nervous system (CNS) and Schwann cells in the peripheral nerve system (PNS). It allows fast and efficient propagation of electrical impulses along axons, thereby modulating various neuronal circuits (McKenzie et al., 2014; Etxeberria et al., 2016). During development, several cell adhesion molecules (CAMs) mediate a complex set of dynamic intercellular interactions between myelinating glia and their underlying axons (Pan and Chan, 2017). These axoglial systems are thought to be involved in various stages in the formation of the myelin sheath, including axonal selection, membrane ensheathment and wrapping, longitudinal growth of the myelin unit, and segregation of the axonal membrane into distinct domains, which is required for saltatory conduction (Barros et al., 2009; Snaidero et al., 2014; Rasband and Peles, 2015; Elazar et al., 2019). However, oligodendrocytes and their underlying axons express a relatively large number of CAMs (Zhang et al., 2014; Sharma et al., 2015), making it challenging to decipher the role specific molecules have in myelination. Furthermore, it is presently unclear whether the function of axoglial CAMs in CNS myelination is at all necessary, as oligodendrocytes are able to ensheath nanofibers, which lack specific axonal adhesive molecules (Lee et al., 2012; Bechler et al., 2015).

Distinct axoglial adhesion complexes are located along the internodes, which reside beneath the compact myelin, and at the paranodal junctions that are formed between the terminal loops of the myelin sheath and the axon. At the paranodal junction, intercellular contact is mediated by glial neurofascin 155 (NF155) and a neuronal complex of Caspr and contactin (Einheber et al., 1997; Menegoz et al., 1997; Rios et al., 2000; Tait et al., 2000; Charles et al., 2002). During myelination, Caspr and NF155 are first clustered at initial contact sites between oligodendrocyte processes and the axon, but then redistribute from the internodes to the forming paranodal junction in a spiral pattern that corresponds to each turn of the myelin sheath (Eisenbach et al., 2009; Pedraza et al., 2009). While the absence of these molecules results in the detachment of the paranodal loops from the axon, it did not affect myelin membrane ensheathment (Bhat et al., 2001; Zonta et al., 2008), suggesting that axoglial contact at the paranodes is not required for myelination. Along the internode, the interaction between myelinating glial cells and the axon is mediated by binding of glial cell adhesion molecule 4 (*Cadm4*), also known as synaptic CAM (SynCAM) or Nectin-like (Necl) adhesion molecule, to axonal *Cadm2* and *Cadm3* (Maurel et al., 2007; Spiegel et al., 2007). However, oligodendrocytes form normal myelin in mice lacking either the *Cadm4* (Zhu et al., 2013; Elazar et al., 2019) or *Cadm3* (Park et al., 2008;

<sup>1</sup>Department of Molecular Cell Biology, Weizmann Institute of Science, Rehovot, Israel; <sup>2</sup>Electron Microscopy Unit, Weizmann Institute of Science, Rehovot, Israel; <sup>3</sup>Department of Veterinary Resources, Weizmann Institute of Science, Rehovot, Israel.

Correspondence to Elior Peles: [peles@weizmann.ac.il](mailto:peles@weizmann.ac.il).

© 2019 Elazar et al. This article is distributed under the terms of an Attribution–Noncommercial–Share Alike–No Mirror Sites license for the first six months after the publication date (see <http://www.rupress.org/terms/>). After six months it is available under a Creative Commons License (Attribution–Noncommercial–Share Alike 4.0 International license, as described at <https://creativecommons.org/licenses/by-nc-sa/4.0/>).

unpublished data) genes, suggesting that Cadm proteins are dispensable for CNS myelination. These observations may also indicate the presence of compensatory CAMs that mediate redundant axon–glia interaction along the internodes. A potential candidate is myelin-associated glycoprotein (MAG), an immunoglobulin superfamily member that is located with Cadm4 at the adaxonal (inner) membrane facing the axon in the CNS and the PNS (Bartsch et al., 1989; Trapp et al., 1989) and is present on oligodendrocyte processes during the initial stages of ensheathment (Bartsch et al., 1989). In line with a possible functional redundancy between Cadm4 and MAG, genetic deletion of the latter in mice had largely no effect on either PNS or CNS myelination (Li et al., 1994; Montag et al., 1994). Notably, while Cadm4–Cadm3 and NF155–Caspr/contactin complexes represent internodal and paranodal adhesion systems, respectively, MAG may contribute to axoglial adhesion at both domains (Marcus et al., 2002; McGonigal et al., 2019).

We have recently shown that increased expression of the extracellular domain of Cadm4 in oligodendrocytes impaired myelin targeting, membrane wrapping, and lateral extension of the myelin sheath (Elazar et al., 2019), indicating that axon–glia adhesion should be tightly regulated during myelination. Given the presence of multiple axoglial CAMs, we reasoned that these molecules should have overlapping functions. Here we tested this idea by genetically ablating Cadm4 together with MAG or with Caspr. We found that accurate ensheathment by oligodendrocytes depends on the coordinated action of different axoglial adhesion systems that limit membrane overgrowth during CNS myelination.

## Results and discussion

### Combined deletion of Cadm4 and MAG results in myelin and motor abnormalities

To test for a possible functional redundancy between Cadm4 and MAG, we have generated mice lacking both genes (*Cadm4*<sup>-/-</sup>/*Mag*<sup>-/-</sup>) by crossing *Cadm4*<sup>-/-</sup> (Golan et al., 2013) and *Mag*<sup>-/-</sup> (Li et al., 1994) heterozygous mice. The complete absence of Cadm4 and MAG proteins in the progeny was confirmed by Western blot analysis of brain lysates (Fig. 1 A). Double *Cadm4*<sup>-/-</sup>/*Mag*<sup>-/-</sup> mice were viable and had normal life spans but, in contrast to the single *Cadm4*<sup>-/-</sup> or *Mag*<sup>-/-</sup> mutants, exhibited a complex neurological motor deficit. On a horizontal beam, which requires precise foot placing and assesses motor balance and coordination (Luong et al., 2011), *Cadm4*<sup>-/-</sup>/*Mag*<sup>-/-</sup> mice displayed a significantly higher rate of leg slippage from the beam and often dragged their pelvis instead of walking (measured as percentage of pelvis dragging), compared with WT or the single *Cadm4*<sup>-/-</sup> or *Mag*<sup>-/-</sup> mutants (Fig. 1, B–D). Catwalk analysis used to assess motor function and coordination revealed that *Cadm4*<sup>-/-</sup>/*Mag*<sup>-/-</sup> mice had abnormal interpaw coordination between several paw combinations, most notably between the right front and left hind paws (Fig. 1 E). Similarly, double *Cadm4*<sup>-/-</sup>/*Mag*<sup>-/-</sup> mice fell more rapidly from a rotarod compared with WT or the single mutants (Fig. 1 F). In contrast to the prominent motor coordination phenotype, when placed in an open field, *Cadm4*<sup>-/-</sup>/*Mag*<sup>-/-</sup> mice showed general activity levels

and gross locomotor and exploration behavior similar to their littermate controls (not depicted).

To examine the formation of myelin in these mice, we performed immunofluorescence labeling of postnatal day 30 (P30) mice brain sections using an antibody to myelin basic protein (MBP). As depicted in Fig. 1 F, this analysis did not reveal any significant difference in either gross morphology or the presence of myelinated tracts between *Cadm4*<sup>-/-</sup>/*Mag*<sup>-/-</sup> and WT or the single gene deletions (Fig. 1 G). Similarly, EM analysis of the corpus callosum of 3-mo-old mice revealed a slight and insignificant decrease in the number of myelinated axons in *Cadm4*<sup>-/-</sup>/*Mag*<sup>-/-</sup> mice (527 ± 61) compared with WT (637 ± 54), *Cadm4*<sup>-/-</sup> (766 ± 47), or *Mag*<sup>-/-</sup> (638 ± 39) mice (Fig. 1, H and I). Unlike *Cadm4*<sup>-/-</sup> or *Mag*<sup>-/-</sup> mice, mice lacking both genes also exhibit several myelin abnormalities, including myelin outfolds (Fig. 1 J). In contrast, EM analysis of sciatic nerves isolated from 1-mo-old mice demonstrated that peripheral myelin in *Cadm4*<sup>-/-</sup>/*Mag*<sup>-/-</sup> mice was indistinguishable from the other genotypes (Fig. 1, K and L).

### Mice lacking both Cadm4 and MAG exhibit multimyelin profiles

To further examine the ultrastructure of the myelin, we performed EM of both cross and longitudinal sections of the corpus callosum of 3-mo-old mice. We found that the most conspicuous abnormality present in *Cadm4*<sup>-/-</sup>/*Mag*<sup>-/-</sup> mice was the appearance of axons surrounded by multiple myelin sheaths (Fig. 2, A–D). These structures contained double, triple, and often quadruple myelin sheaths, which were frequently interrupted by cytoplasmic pockets that are typically present only at the periaxonal space and the paranodal loops. The frequency of these multimyelinated axon profiles was significantly higher in *Cadm4*<sup>-/-</sup>/*Mag*<sup>-/-</sup> mice (7.8 ± 2.8% per field of view) compared with WT (0.1 ± 0.2%), *Cadm4*<sup>-/-</sup> (0.4 ± 0.4%), or *Mag*<sup>-/-</sup> (1.9 ± 1%) mice (Fig. 2 E). In addition, non-multimyelinated axons in *Cadm4*<sup>-/-</sup>/*Mag*<sup>-/-</sup> mice displayed thicker myelin (i.e., lower g-ratio: 0.66 ± 0.07 compared with 0.726 ± 0.07 in WT mice), with 22% of myelinated profiles having a g-ratio <0.65 compared with 5, 8, and 9% in WT, *Cadm4*<sup>-/-</sup>, and *Mag*<sup>-/-</sup> mice, respectively (Fig. 2 F). We next analyzed longitudinal sections of optic nerves isolated from *Cadm4*<sup>-/-</sup>/*Mag*<sup>-/-</sup> mice. We observed paranodal loops that were present on top (Fig. 2 G) or underneath (Fig. 2 H) compact myelin. To further examine the cellular basis for the formation of double myelin, we followed individual axons by performing 3D reconstruction using a focused ion beam scanning EM (FIB-SEM) on optic nerves isolated from adult *Cadm4*<sup>-/-</sup>/*Mag*<sup>-/-</sup> mice. As depicted in Fig. 2 I, we identified axons that were myelinated by two separate sheaths containing paranodal loops that arose from one sheath and attached on top of another (Fig. 2 I, a–d). These results suggest that multimyelinated axons are formed by the longitudinal overgrowth of the myelin lamellae beneath the forming paranodal junction. Developmental EM analysis of corpus callosum sections obtained from *Mag*<sup>-/-</sup> and *Cadm4*<sup>-/-</sup>/*Mag*<sup>-/-</sup> mice revealed that double myelin is already formed during the first three postnatal weeks (Fig. 2, J–M), indicating that they represent an abnormal growth of the myelin sheath during myelination. The increased number

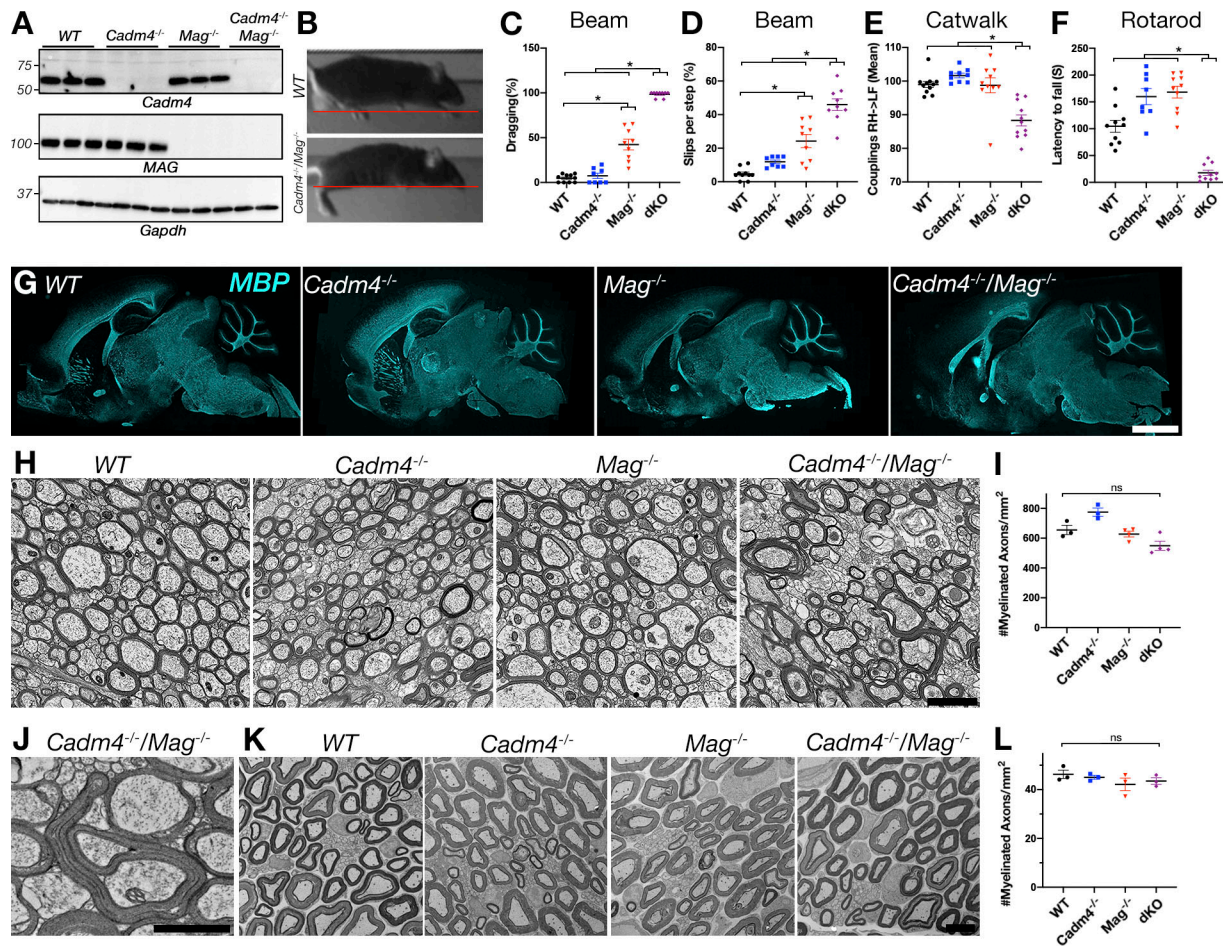


**Figure 1. Deletion of both *Cadm4* and *MAG* results in significant motor defects.** (A) Generation of double mutant mice lacking both *Cadm4* and *MAG*. Western blot analysis of 5–6-mo brains of the indicated genotypes using antibodies to *Cadm4*, *MAG*, and *Gapdh*. The location of MW markers is shown in kilodaltons. (B) Representative image of WT and *Cadm4*<sup>-/-</sup>/*Mag*<sup>-/-</sup> mice drag their pelvis and misplace hindlimb on beam (red line). (C and D) Quantification of the percentage of pelvis dragging (C) and hindlimb misplacement registered (D). Graphs represent mean ± SEM of at least eight mice of each genotype (*n* = 10, 8, 9, 9); \*, *P* < 0.05, one-way ANOVA with Tukey’s multiple comparisons test correction. (E) Gait analysis showing the coupling between right hind and left front limbs of using catwalk paradigm. Graph represents mean ± SEM of at least nine mice of each genotype (*n* = 10, 9, 10, 11); \*, *P* < 0.05, one-way ANOVA with Tukey’s multiple comparisons test correction. (F) Rotarod test of adult mice showing that the double *Cadm4*<sup>-/-</sup>/*Mag*<sup>-/-</sup> mutant mice had a shorter latency to fall compared with single (*Cadm4*<sup>-/-</sup> or *Mag*<sup>-/-</sup>) mutants or WT mice. Graph represents mean ± SEM of at least eight mice of each genotype (*n* = 10, 8, 10, 10); \*, *P* < 0.05, one-way ANOVA with Tukey’s multiple comparisons test correction. Motor analysis was done using 5–6-mo-old (B, C, and F), or 4–5-mo-old (D) mice. (G) Midsagittal sections of P30 brains isolated from the indicated genotypes immunolabeled with antibody to MBP. (H and I) Electron micrographs of corpus callosum sections from 3-mo-old mice of the different genotypes as indicated. The number of myelinated axons in *Cadm4*<sup>-/-</sup>/*Mag*<sup>-/-</sup> mutant mice is comparable to WT animals and the single gene-deleted mice. Number of myelinated axons per square millimeter. Graphs represent mean ± SEM of ≥3,500 axons counted from three mice of each genotype (ns, not significant; *P* > 0.05, one-way ANOVA with Tukey’s multiple comparisons test correction). Note that in contrast to *Cadm4*<sup>-/-</sup> or *Mag*<sup>-/-</sup> mutants, the double mutant shows abnormal myelin profiles. (J) Higher-magnification image showing that *Cadm4*<sup>-/-</sup>/*MAG*<sup>-/-</sup> mice display myelin outfoldings. (K and L) Mice lacking both *Cadm4* and *MAG* display normal PNS myelin. Electron micrographs of cross sections of sciatic nerves from 1-mo-old mice of the different genotypes as indicated. (L) Number of myelinated axons per square millimeter. Graphs represent mean ± SEM of ≥700 axons counted from three mice of each genotype (ns, not significant; *P* > 0.05, one-way ANOVA with Tukey’s multiple comparisons test correction). Scale bars, 2 mm (G); 2 μm (H); 1 μm (J); 5 μm (K).

of multiple myelin profiles in the absence of both *Cadm4* and *MAG* reveals that these two internodal CAMs play compensatory roles in keeping the inner membrane of oligodendrocytes in register with the axons, as previously suggested for *MAG* (Li et al., 1994; Montag et al., 1994).

**Deletion of *Cadm4* and *Caspr* phenocopies the multimyelinated profiles of *Cadm4*<sup>-/-</sup>/*Mag*<sup>-/-</sup>**

Longitudinal overgrowth of the myelin membrane in *Cadm4*<sup>-/-</sup>/*Mag*<sup>-/-</sup> mice (Fig. 2, G–I), and hence the formation of multiple

myelin profiles, may depend on loosening of the attachments of the paranodal loops to the axon, as detected in several paranodal mutant mice (Dupree et al., 1998; Bhat et al., 2001). To begin to clarify how the deletion of two internodal CAMs results in such a phenotype, we labeled mice brain sections and myelinated spinal cord cultures using different combinations of *MAG*, *Cadm4*, and *Caspr* antibodies. We found that in contrast to the PNS (Maurel et al., 2007; Spiegel et al., 2007), *MAG*, but not *Cadm4*, is enriched at the paranodes (Fig. S1), suggesting that it may be involved in paranodal adhesion. This idea is in line with

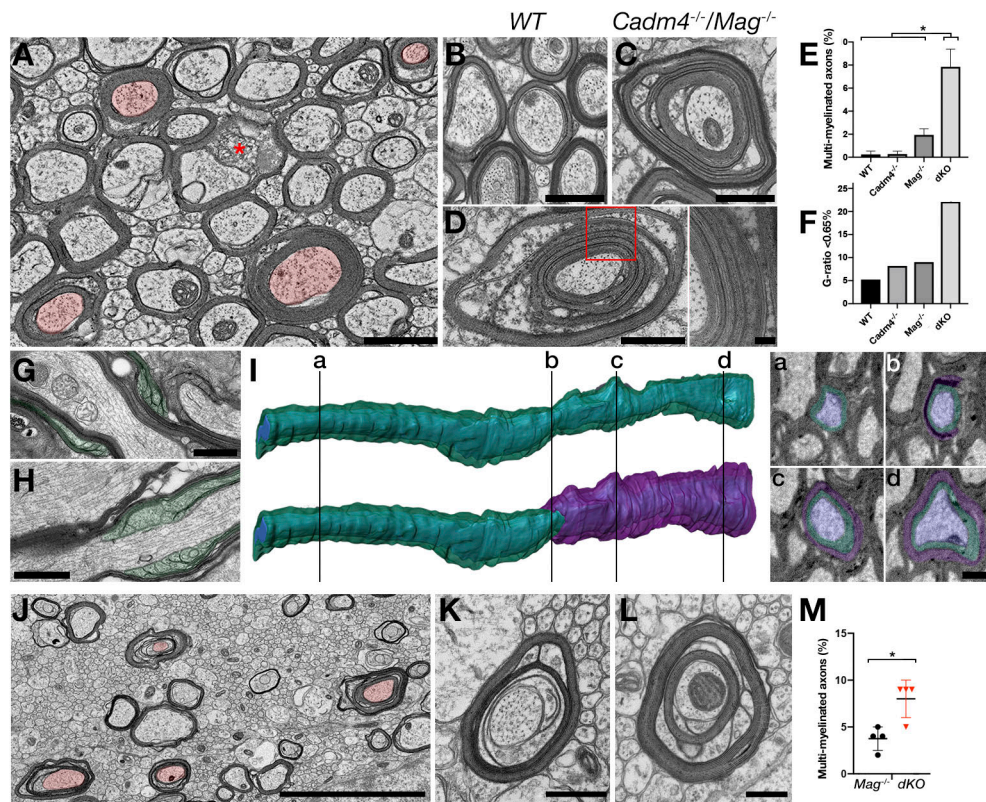


**Figure 2. Mice lacking both *Cadm4* and MAG exhibit multimyelinated axons.** (A) Low-magnification electron micrographs of midsagittal sections of the corpus callosum of 3-mo-old *Cadm4*<sup>-/-</sup>/*MAG*<sup>-/-</sup> mice displaying multiple double-myelinated axons (colored). (B and C) Representative images of myelinated axons from corpus callosum of WT (B) and *Cadm4*<sup>-/-</sup>/*Mag*<sup>-/-</sup> (C) mice. (D) High-magnification of corpus callosum of 3-mo-old *Cadm4*<sup>-/-</sup>/*Mag*<sup>-/-</sup> displaying axonal ensheathment by multiple myelin units, higher-magnification image of the boxed area is shown. (E) Percentage of multimyelinated profiles out of myelinated axons in the corpus callosum in the different genotypes. Graph represents mean ± SEM of ≥3,500 axons counted from at least three mice of each genotype (\*, *P* < 0.05, one-way ANOVA with Tukey's multiple comparisons test correction). (F) Percentage of axons displaying a G-ratio < 0.65 in the different genotypes. Graph represents ≥500 axons counted from at least three mice of each genotype. (G and H) Longitudinal sections of optic nerves of 3-mo-old *Cadm4*<sup>-/-</sup>/*Mag*<sup>-/-</sup> mice displaying several abnormalities, including external attachment of the paranodal loops on compact myelin (G) and presence of paranodal loops underneath compact myelin (H). (I) 3D reconstruction of a serial block-face FIB-SEM of a *Cadm4*<sup>-/-</sup>/*Mag*<sup>-/-</sup> optic nerve (4.9 × 8.4 × 14.4 μm) displaying a double-myelinated axon (blue); upper row represents one myelin unit (cyan), and bottom row displays the merged double-myelinated axon row represents an additional myelin unit (purple); alphabet in 3D reconstruction refers to cross sections. (J) Multimyelinated axons appear early in development. Low-magnification electron micrographs of midsagittal sections of the corpus callosum from P21 mice displaying multiple double-myelinated axons (colored). (K and L) Representative images of myelinated axons from corpus callosum of double-knockout mice. (M) Percentage of multimyelinated profiles out of myelinated axons in the corpus callosum in the different genotypes. Graph represents mean ± SEM of ≥2,500 axons counted from four mice of each genotype (\*, *P* < 0.05, Student's *t* test). Scale bars, 1 μm (A, G, and H), 0.5 μm (B, C, D, I, K, and L); 0.1 μm (D, inset); 5 μm (J).

previous studies showing that, in addition to mediating axoglial adhesion along the internodes, MAG regulates the formation and integrity of the paranodal junction (Marcus et al., 2002). We reasoned that if the contribution of MAG to the *Cadm4*<sup>-/-</sup>/*Mag*<sup>-/-</sup> phenotype is due to its role in paranodal adhesion, one should expect to obtain a similar phenotype in mice lacking *Cadm4* and other paranodal CAMs. To test this possibility, we reduced both internodal and paranodal adhesion by removing *Cadm4* and the paranodal protein *Caspr* (Fig. 3 A). *Cadm4*<sup>-/-</sup>/*Caspr*<sup>-/-</sup> mice were generated by crossing heterozygous *Cadm4*<sup>-/-</sup> (Golan et al., 2013) and *Caspr*<sup>-/-</sup> (Gollan et al., 2003) mice, and the absence of both proteins was assessed by immunolabeling of P45 optic nerves (Fig. 3 B). *Cadm4*<sup>-/-</sup>/*Caspr*<sup>-/-</sup> mice displayed a more severe neurological phenotype than *Caspr*<sup>-/-</sup> or *Cadm4*<sup>-/-</sup>, resulting in premature death starting at P15. In mice surviving >2 wk, the neurological abnormalities deteriorated over time, resulting in complete hindlimb paralysis at P40.

EM analyses of sciatic nerve cross sections obtained from *Caspr*<sup>-/-</sup> and *Cadm4*<sup>-/-</sup>/*Caspr*<sup>-/-</sup> mice at P40 showed the presence of normal myelin profiles in both genotypes (Fig. 3 C). In contrast, analysis of optic nerves isolated from WT and single and double gene deletion demonstrated that *Cadm4*<sup>-/-</sup>/*Caspr*<sup>-/-</sup> exhibited a significant reduction in the density of myelinated axons (414 ± 37) compared with *Cadm4*<sup>-/-</sup> (606 ± 86) and *Caspr*<sup>-/-</sup> (550 ± 44) mutants or WT mice (650 ± 80; Fig. 3, D and E). Consistent with our hypothesis that reduced adhesion at the internode and the paranode will result in myelin overgrowth, *Cadm4*<sup>-/-</sup>/*Caspr*<sup>-/-</sup> mutant mice exhibited multimyelin abnormalities that phenocopied that of mice lacking *Cadm4* and MAG (Fig. 4, A–E). *Cadm4*<sup>-/-</sup>/*Caspr*<sup>-/-</sup> mutant mice formed a significantly higher percentage of aberrant myelin, with double-myelinated axons in both the optic nerve (13.8 ± 3.1) and the corpus callosum (9.7 ± 2.2) compared with WT (0 ± 0 in both), *Cadm4*<sup>-/-</sup> (0 ± 0 and 0.32 ± 0.2 in optic nerve and corpus

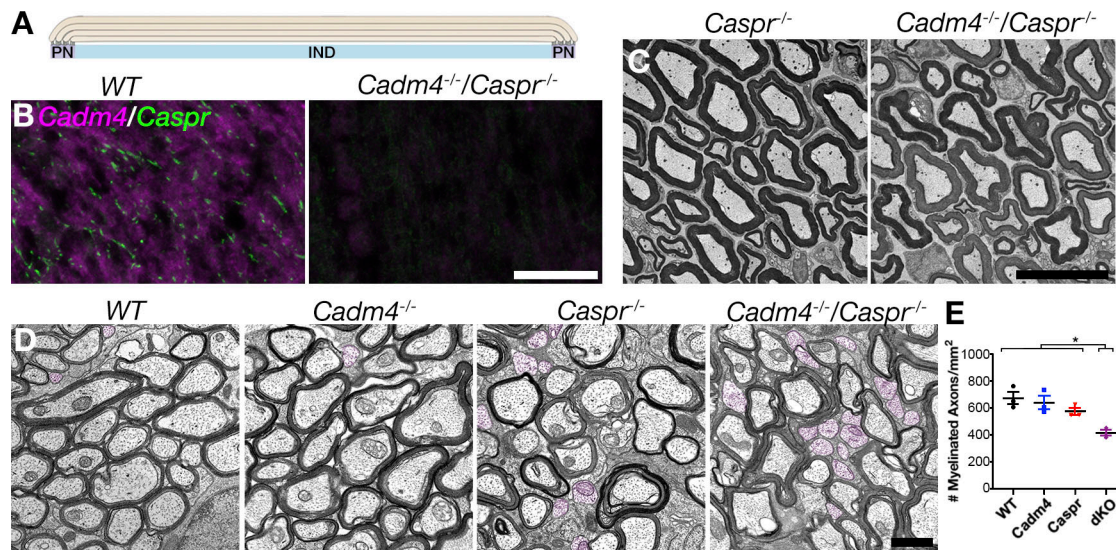


**Figure 3. *Cadm4<sup>-/-</sup>/Caspr<sup>-/-</sup>* mutants exhibit severe neurological abnormalities and CNS hypomyelination.** (A) Schematic representation of myelin adhesion system in longitudinal view. Internodal (IND) and paranodal (PN) adhesion zones containing *Cadm4* and *Caspr*, respectively, are indicated. (B) Immunofluorescence labeling of optic nerve sections isolated from 1.5-mo-old WT or *Cadm4<sup>-/-</sup>/Caspr<sup>-/-</sup>* mice using antibodies to *Cadm4* and *Caspr*. (C) Absence of *Cadm4* and *Caspr* did not result in peripheral myelin abnormality. Electron micrographs showing cross sections of 1-mo-old sciatic nerves from *Caspr<sup>-/-</sup>* and *Cadm4<sup>-/-</sup>/Caspr<sup>-/-</sup>* mice. (D) Double *Cadm4<sup>-/-</sup>/Caspr<sup>-/-</sup>* mutant mice exhibit CNS hypomyelination. Electron micrographs of cross sections of optic nerve from 1.5-mo-olds of indicated genotypes (nonmyelinated axons labeled in magenta). (E) Number of myelinated axons per square millimeter in the optic nerve. Graphs represent mean ± SEM of ≥2,000 axons counted from three mice of each genotype (\*,  $P < 0.05$ , one-way ANOVA with Dunnett's multiple comparisons test correction). Scale bars, 20 μm (B); 10 μm (C); 1 μm (D).

callosum, respectively), and *Caspr<sup>-/-</sup>* ( $5.2 \pm 2.5$  and  $3.3 \pm 0.5$ ) mice (Fig. 4, F and G). Longitudinal sections of WT (Fig. 4 H) and *Cadm4<sup>-/-</sup>/Caspr<sup>-/-</sup>* nerves revealed what appeared to be overgrowth of paranodal loops over existing compact myelin (Fig. 4 I), as well as the presence of compact myelin covering paranodal loops that contacted the axon (Fig. 4, J and K). 3D reconstruction of serial sections obtained from *Cadm4<sup>-/-</sup>/Caspr<sup>-/-</sup>* optic nerves using FIB-SEM revealed two sheaths growing on top of each other, resulting in two paranodal junctions forming either on top or beneath compact myelin (Fig. 4, L and M, a–f). These multi-myelin profiles recapitulate those detected in *Cadm4<sup>-/-</sup>/Mag<sup>-/-</sup>* mice, further supporting the interpretation that the combined reduction in paranodal and internodal adhesion results in overgrowth of the myelin sheath. Interestingly, even in the absence of paranodal and internodal axoglial CAMs, the paranodal loops still formed, suggesting that they are being held together by an additional adhesion system.

Our findings reveal that the coordinated action of several axoglial adhesion systems controls the growth of the myelin membrane in the CNS. In the absence of this adhesion, myelin targeting and axonal ensheathment still occurs, but the lateral elongation of the myelin sheath is unreliable, demonstrating that axoglial CAMs limit the lateral overgrowth of oligodendrocyte myelin. According to the prevailing model of CNS myelination (Snidero et al., 2014), the inner membrane of the myelin sheath moves around the axon underneath previously formed myelin lamellae, which grow laterally. During this process, internodal CAMs mediate intercellular contact between the inner myelin lip and the axon (Bartsch et al., 1989; Elazar et al., 2019), while paranodal CAMs

mediate the interaction between the axon and the paranodal loops that are forming at the edge of the laterally growing myelin sheath (Eisenbach et al., 2009; Pedraza et al., 2009). We propose that the synergistic action of these internodal and paranodal CAMs regulates the growth of the myelin sheath. In *Cadm4<sup>-/-</sup>* mice, reduced internodal adhesion does not result in myelin overgrowth due to the presence of paranodal adhesion that attaches the myelin sheath to the axon. In paranodal mutants such as *Caspr<sup>-/-</sup>* (Bhat et al., 2001) or mice lacking ceramide galactosyltransferase (Dupree et al., 1998), paranodal adhesion is impaired, resulting in only limited generation of double myelin profiles due to the presence of internodal adhesion by *Cadm4*. In contrast, by reducing both internodal and paranodal adhesion in *Cadm4<sup>-/-</sup>/Caspr<sup>-/-</sup>* mice, the growth of the inner myelin membrane is not limited to the axons, and it extends beneath the detached paranodal loops and could continue to grow either over or under an adjacent forming myelin segment (Fig. 5). Notably, our data do not exclude the possibility that some of the double myelin profiles observed are not the result of longitudinal overgrowth of the inner lip, but rather are formed by direct oligodendrocyte ensheathment of preexisting myelin. In this case, *Cadm4*, but likely not *MAG* (Chong et al., 2012), may inhibit wrapping of other myelin segments. Surprisingly, this does not affect myelin wrapping by Schwann cells, suggesting that in peripheral nerves the basal lamina and additional CAMs present at the Schwann cell microvilli that contact the nodes (Eshed et al., 2005; Bang et al., 2018) are sufficient to keep the growing myelin membrane in register with the axon.

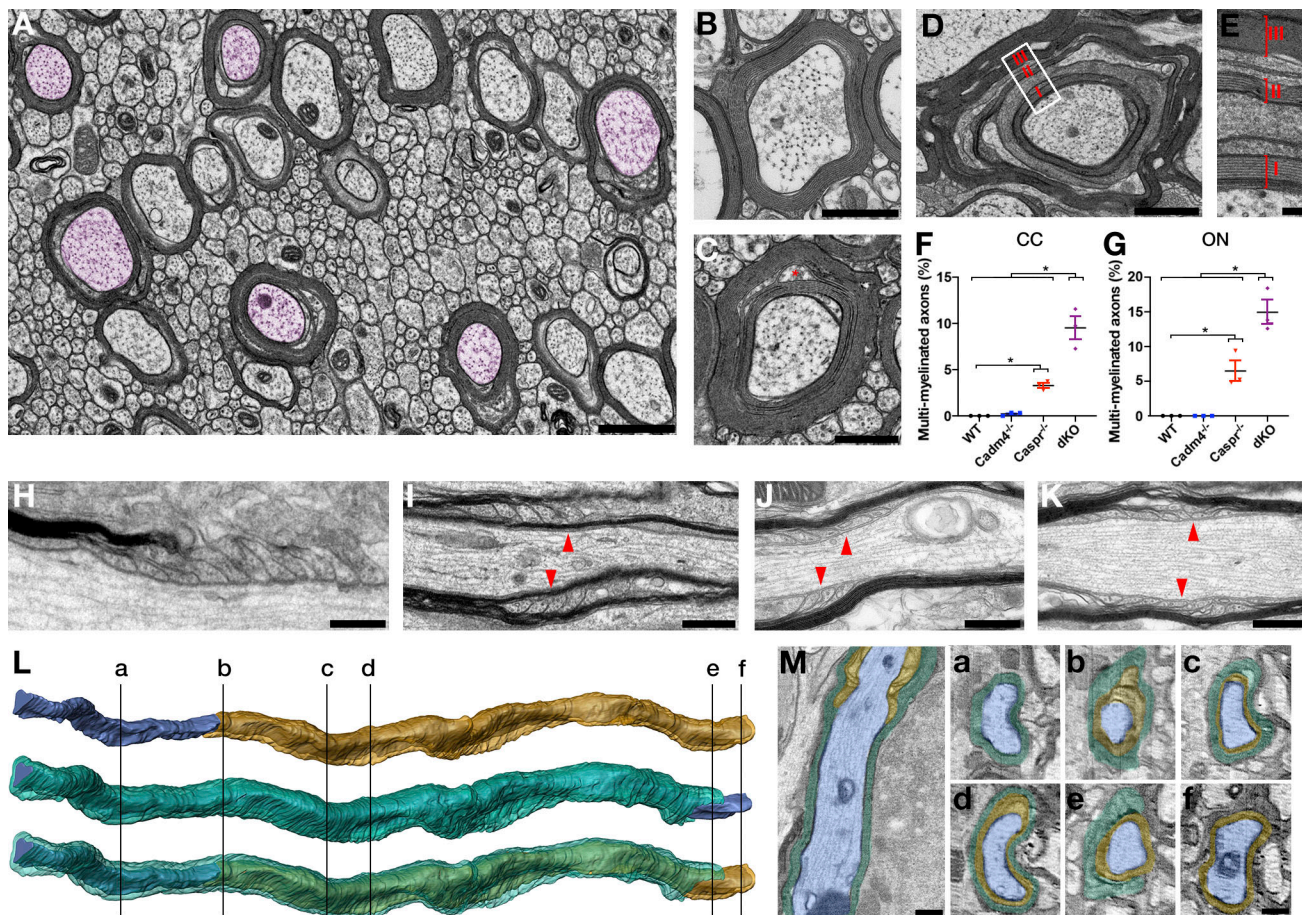


**Figure 4. Deletion of *Cadm4* and *Caspr* results in the formation multimyelin profiles.** (A) Low-magnification electron micrographs of mid-sagittal sections of the corpus callosum of 1.5-mo-old *Cadm4*<sup>-/-</sup>/*Caspr*<sup>-/-</sup> mice displaying multiple double-myelinated axons (colored). (B and C) Images of myelinated axons from corpus callosum of WT (B) and *Cadm4*<sup>-/-</sup>/*Caspr*<sup>-/-</sup> (C). Asterisk marks the presence of a mesaxonal tongue within compact myelin. (D) Spinal cord section of 1.5-mo-old double-knockout mouse displaying axonal ensheathment by multiple myelin units (marked I–III). (E) Higher-magnification image of the boxed area shown in D. (F and G) Percentage of multimyelinated profiles out of myelinated axons in the corpus callosum (CC; F) and optic nerve (ON; G) found in the different genotypes. Graphs represent mean ± SEM of ≥2,000 axons counted from three mice of each genotype (\*, P < 0.05, one-way ANOVA with Tukey's multiple comparisons test correction). (H–K) Longitudinal sections of optic nerves from P21–P25 WT (H) and *Cadm4*<sup>-/-</sup>/*Caspr*<sup>-/-</sup> (K–M) mice. The latter exhibit several abnormalities, including external attachment of the paranodal loops on compact myelin (arrowheads in K) and presence of paranodal loops underneath compact myelin (arrowheads in K–M). (L and M) Serial block-face FIB-SEM of a *Cadm4*<sup>-/-</sup>/*Caspr*<sup>-/-</sup> optic nerve (7.7 × 28.6 × 10.35 μm). (L) 3D reconstruction of a *Cadm4*<sup>-/-</sup>/*Caspr*<sup>-/-</sup> optic nerve displaying a double-myelinated axon (blue); upper row represents one myelin unit (yellow), middle row represents an additional myelin unit (green), and bottom row displays the merged double-myelinated axon; alphabet in 3D reconstruction refers to cross sections. (M) Longitudinal section of the multimyelinated axon (blue) presented in L; note the presence of paranodal loops (yellow) underneath compact myelin (green). Representative images of cross sections in different z-planes along the 3D reconstruction depicted as a–f in L. Scale bars, 2 μm (A); 1 μm (D); 0.5 μm (B, C, H–K, M, and a–f); 0.1 μm (E).

## Materials and methods

### Animals

*Cadm4*<sup>-/-</sup>, *Mag*<sup>-/-</sup>, and *Caspr*<sup>-/-</sup> mice were previously described (Li et al., 1994; Gollan et al., 2003; Golan et al., 2013). *Cadm4*<sup>-/-</sup> and *Mag*<sup>-/-</sup> mice were bred on a C57BL/6 background (Jackson Laboratory), while *Caspr*<sup>-/-</sup> mice were bred on an ICR background (Jackson Laboratory). Homozygous *Cadm4*<sup>-/-</sup>/*Mag*<sup>-/-</sup> and *Cadm4*<sup>-/-</sup>/*Caspr*<sup>-/-</sup> mice were obtained by a conventional breeding scheme. Genotypes were determined by performing PCR on genomic DNA extracted from mice tails or sciatic nerves using previously described primers. Genotyping was done by standard PCR using the following primers: *Cadm4* WT, 5'-GGCAGTTCTGATCCAGCATC-3' and 5'-ATCAGAGGACAGCTCATGAG-3'; *Cadm4*<sup>-/-</sup>, 5'-CGCAGTTCTGATCCAGCATC-3' and 5'-GGC

AGGAGGGTTGCCATGA-3'; *Mag*<sup>-/-</sup> 5'-TGCCGCTGTTTTGGA TAA-3', 5'-CGCCTCGGAAATAGTATTTG-3', and 5'-CTTGGGTGGAGAGGCTATTC-3'; *Caspr* WT, 5'-GAGAGGGAAGGGTGGATAAGGAC-3' and 5'-ATTGCGGAGCGCTGGGAGAGG-3'; *Caspr*<sup>-/-</sup> 5'-ATTTCCCAACGGCAGGTT-3' and 5'-TCGCCCTTCTTGACGAGTTTC-3'. Both male and female animals were used in the study, with no detectable difference in myelin morphology. Animals were maintained in the animal facility at the Weizmann Institute and housed in a temperature-controlled animal room with a 12-h light/dark cycle. Water and food were available ad libitum. All experiments were performed in compliance with the relevant laws and institutional guidelines and were approved by the Weizmann Institute's Animal Care and Use Committee.

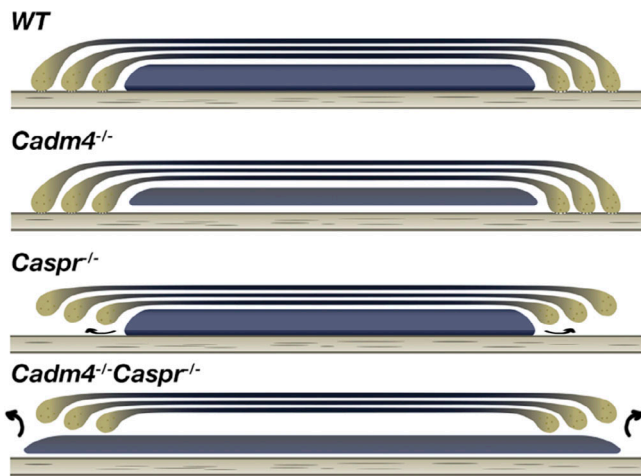


**Figure 5. A summary model of myelination in the absence of internodal and paranodal adhesion.** Schematic representation (longitudinal view) of the forming myelin unit in the indicated genotypes. In WT mice, the inner myelin membrane along the internode (blue), as well as the flanking paranodal loops (yellow), are contacting the axon (dark line represents adhesion of the inner membrane to the axon). In the absence of internodal adhesion (*Cadm4*<sup>-/-</sup>), unregulated lateral growth of the inner membrane is prevented by the paranodes. In the absence of paranodal adhesion (*Caspr*<sup>-/-</sup>), internodal adhesion generally limits lateral membrane overgrowth (limited extension of the myelin beneath the paranodal loops is marked by small arrows). The absence of both internodal and paranodal adhesion results in longitudinal growth of the myelin either over or under an adjacent forming myelin segment (arrows), resulting in the formation of multimyelin profiles.

For motor tests, a total of 42 male and female mice 4–6 mo old were evaluated (10 male WT, 7 male and 3 female *Cadm4*<sup>-/-</sup>, 3 male and 7 female *Mag*<sup>-/-</sup>, and 6 male and 6 female *Cadm4*<sup>-/-</sup>/*Mag*<sup>-/-</sup>). In each behavioral experiment, animals were evaluated one at a time. The behavioral studies were performed in the behavioral Laboratory in the animal facility at the Weizmann Institute. Rotarod was done using a standard rotarod apparatus (Panlab) as previously described (Novak et al., 2011). Coordination motor ability was assessed by training mice to walk on a horizontal beam (35-mm width, 50-cm length) raised 30 cm above the working surface to get back to their home cage. Trials consisted of mice forced to cross a narrow beam (6 mm wide) to get back to their home cages uninterrupted five times. Test sessions were video recorded using an overhead camera and manually scored for time spent on the beam and slips per step percentage, together with groin dragging. Gait was analyzed using a Catwalk gait automatic analyzer (CatWalk; Noldus Information Technology). The position, timing, and dimensions of each footfall were recorded by a video camera positioned underneath a glass plate.

### Immunocytochemistry

Mice were anesthetized and perfused with 2% PFA/PBS. Brains and optic nerves were isolated and postfixed on ice for 30 min. For immunofluorescence, tissues were incubated in 30% sucrose/PBS at 4°C overnight, embedded in optimal cutting temperature medium, and sectioned (12 μm). Sections were washed with PBS and blocked with PBS containing 5% normal goat serum, 0.5% Triton X-100, and 0.05% sodium azide for 1 h at RT.

Samples were incubated overnight at 4°C with primary antibodies diluted in PBS containing 5% normal goat serum, 0.5% Triton X-100, and 0.05% sodium azide; washed three times in PBS; incubated for 1 h with secondary antibodies; washed in PBS; and mounted with Fluoromount-G. Immunohistochemistry of paraffin sections (6 μm) was performed after deparaffinization, rehydration (graded ethanol solutions), and antigen retrieval (10 mmol/liter citrate, pH 6.0, at 95°C for 10–15 min). Immunofluorescence labeling was done essentially as described above. For immunocytochemistry, cells were fixed using 4% PFA for 10 min at RT and subsequently washed with PBS and immunolabeled as described above. Images were acquired at room temperature using an LSM700 confocal microscope (Carl Zeiss) by using a 40×/1.2-NA lens imaged with Carl Zeiss immersol W 2010, a 63×/1.4-NA lens imaged with Carl Zeiss immersol 518F, or a Panoramic digital slide scanner (3DHISTECH) using a 20×/0.8-NA air lens. For image analysis, images were taken in equivalent spatial distribution from all slides. Image analysis was performed using ImageJ and ZEN 2011 (Carl Zeiss) software. The following primary antibodies were used for immunostaining: rat anti-MBP (1:300, R&D Systems), mouse anti-Cadm4 (1:500, NeuroMab), rabbit anti-Cadm4 (1:500), and rabbit anti-Caspr (1:500). Secondary antibodies coupled to Dylight 405, 488, Cy3, Dylight 647, Cy5, and Cy3 were obtained from Jackson ImmunoResearch.

### EM

Mice were anesthetized and perfused with a fixative containing 4% PFA, 2.5% glutaraldehyde, and 0.1 M cacodylate buffer. Brains and spinal cords were isolated and incubated in the fixative overnight at room temperature and processed as previously described (Yang et al., 2016). Samples were examined using a Tecnai Spirit or T12 transmission EM equipped with a FEI Eagle camera or a Gatan ES500W Erlangshen camera, respectively. EM micrographs were analyzed using computer-assisted ImageJ analysis software, for axon diameter and total outer axon diameter containing myelin. G-ratio was calculated by dividing the measured inner axonal diameter by the measured total outer axonal diameter. For FIB-SEM, samples were fixed (Yang et al., 2016) and embedded in Epoxy resin (Agar Scientific). FIB-SEM was performed on a Crossbeam 550 FIB-SEM (Carl Zeiss). Specimens were coated (6 nm) with a conductive layer of iridium and prepared with sputter coating (Safematic). Ion beam current at 20 pA to 30 nA was used. Scanning EM images were acquired at 2 kV, 490 pA, with Inlens detector and noise reduction of line averaging ( $n = 80$ ). Slicing was performed with an ion beam of 700 pA, by Serial Surface Imaging algorithm SmartFIB. Image series of consecutive sections were collected using an isotropic voxel size of  $7 \times 7 \times 7$  nm. Image processing was performed by Fiji (National Institutes of Health). FIB-SEM image stacks were aligned and segmented in Microscopy Image Browser (University of Helsinki) and 3D reconstructed in Amira-Avizo SW (Thermo Fisher Scientific).

### Myelinating spinal cord cultures

Spinal cords isolated from genotyped embryonic day 13.5 mice embryos were transferred to HBSS and dissociated using 0.25%

trypsin and 0.1% collagenase. Cells were collected, resuspended in spinal cord plating medium (DMEM containing 25% horse serum, 25% HBSS, and 4 mM glutamine), and plated (300,000/13 mm coverslip) on 0.1% poly-L-lysine-coated coverslips. 3 h after seeding, the medium was changed to differentiation medium (DMEM containing 0.5% hormone mix [1 mg/ml apo-transferrin, 20 mM putrescine, 4 mM progesterone, and 6 mM selenium], 10 ng/ml biotin, and 50 nM hydrocortisone). Insulin (10 mg/ml) was added to the differentiation medium for the first 12–14 d. Medium was changed every other day for 28 d.

### Western blots

Mouse brains were lysed in RIPA buffer (10 mM Tris-Cl, pH 8.0, 1 mM EDTA, 1% Triton X-100, 0.1% sodium deoxycholate, 0.1% SDS, 140 mM NaCl, and 1 mM PMSF) supplemented with protease inhibitors. Equal amounts of protein were loaded onto a 10% SDS-PAGE gel and transferred to polyvinylidene difluoride membrane. Membranes were blotted with antibodies to Cadm4, MAG, and Gapdh, and then incubated with HRP-conjugated secondary antibodies. Blots were developed by ECL and imaged on a Bio-Rad ChemiDOC.

### Statistical analyses

Data are presented as the mean  $\pm$  SEM or average  $\pm$  SD. Statistical analyses were performed using an unpaired Student's *t* test with two tails or one-way ANOVA with Tukey's or Dunnett's multiple comparisons test correction. For in vivo experiments, sample size was not predetermined but was based on similar studies in the field.

### Online supplemental material

Fig. S1 shows that MAG exhibits higher paranodal localization than Cadm4.

## Acknowledgments

We thank Jeff Dupree and Mika Simons for discussions.

This work was supported by the National Institutes of Health (R01NS097428), the Dr. Miriam and Sheldon G. Adelson Medical Research Foundation, the National American Brain Foundation, Lilly Fulop Fund for Multiple Sclerosis Research, Estate of David Georges Eskinazi, and research grants from Dahlia and Philip Lawee, Gary Clayman, and Ellie Adiel. E. Pelez is the Incumbent of the Hanna Hertz Professorial Chair for Multiple Sclerosis and Neuroscience.

The authors declare no competing financial interests.

Author contributions: N. Elazar and E. Peles: conceptualization; N. Elazar, A. Vainshtein, Y. Eshed-Eisenbach, K. Rechav, and Y.M. Tsoory: investigation. N. Elazar and E. Peles: manuscript preparation. E. Peles secured funding and supervised the project.

Submitted: 16 June 2019

Revised: 10 July 2019

Accepted: 11 July 2019

## References

- Bang, M.L., A. Vainshtein, H.J. Yang, Y. Eshed-Eisenbach, J. Devaux, H.B. Werner, and E. Peles. 2018. Glial M6B stabilizes the axonal membrane at peripheral nodes of Ranvier. *Glia*. 66:801–812. <https://doi.org/10.1002/glia.23285>
- Barros, C.S., T. Nguyen, K.S. Spencer, A. Nishiyama, H. Colognato, and U. Müller. 2009. Beta1 integrins are required for normal CNS myelination and promote AKT-dependent myelin outgrowth. *Development*. 136: 2717–2724. <https://doi.org/10.1242/dev.038679>
- Bartsch, U., F. Kirchhoff, and M. Schachner. 1989. Immunohistological localization of the adhesion molecules L1, N-CAM, and MAG in the developing and adult optic nerve of mice. *J. Comp. Neurol.* 284:451–462. <https://doi.org/10.1002/cne.902840310>
- Bechler, M.E., L. Byrne, and C. Ffrench-Constant. 2015. CNS Myelin Sheath Lengths Are an Intrinsic Property of Oligodendrocytes. *Curr. Biol.* 25: 2411–2416. <https://doi.org/10.1016/j.cub.2015.07.056>
- Bhat, M.A., J.C. Rios, Y. Lu, G.P. Garcia-Fresco, W. Ching, M. St Martin, J. Li, S. Einheber, M. Chesler, J. Rosenbluth, et al. 2001. Axon-glia interactions and the domain organization of myelinated axons requires neurexin IV/Caspr/Paranodin. *Neuron*. 30:369–383. [https://doi.org/10.1016/S0896-6273\(01\)00294-X](https://doi.org/10.1016/S0896-6273(01)00294-X)
- Charles, P., S. Tait, C. Faivre-Sarrailh, G. Barbin, F. Gunn-Moore, N. Denisenko-Nehrbass, A.M. Guennoc, J.A. Girault, P.J. Brophy, and C. Lubetzki. 2002. Neurofascin is a glial receptor for the paranodin/Caspr-contactin axonal complex at the axoglial junction. *Curr. Biol.* 12: 217–220. [https://doi.org/10.1016/S0960-9822\(01\)00680-7](https://doi.org/10.1016/S0960-9822(01)00680-7)
- Chong, S.Y., S.S. Rosenberg, S.P. Fancy, C. Zhao, Y.A. Shen, A.T. Hahn, A.W. McGee, X. Xu, B. Zheng, L.I. Zhang, et al. 2012. Neurite outgrowth inhibitor Nogo-A establishes spatial segregation and extent of oligodendrocyte myelination. *Proc. Natl. Acad. Sci. USA*. 109:1299–1304. <https://doi.org/10.1073/pnas.1113540109>
- Dupree, J.L., T. Coetzee, K. Suzuki, and B. Popko. 1998. Myelin abnormalities in mice deficient in galactocerebroside and sulfatide. *J. Neurocytol.* 27: 649–659. <https://doi.org/10.1023/A:1006908013972>
- Einheber, S., G. Zanazzi, W. Ching, S. Scherer, T.A. Milner, E. Peles, and J.L. Salzer. 1997. The axonal membrane protein Caspr, a homologue of neurexin IV, is a component of the septate-like paranodal junctions that assemble during myelination. *J. Cell Biol.* 139:1495–1506. <https://doi.org/10.1083/jcb.139.6.1495>
- Eisenbach, M., E. Kartvelishvily, Y. Eshed-Eisenbach, T. Watkins, A. Sorensen, C. Thomson, B. Ranscht, S.C. Barnett, P. Brophy, and E. Peles. 2009. Differential clustering of Caspr by oligodendrocytes and Schwann cells. *J. Neurosci. Res.* 87:3492–3501. <https://doi.org/10.1002/jnr.22157>
- Elazar, N., A. Vainshtein, N. Golan, B. Vijayaragavan, N. Schaeren-Wiemers, Y. Eshed-Eisenbach, and E. Peles. 2019. Axoglial Adhesion by Cadm4 Regulates CNS Myelination. *Neuron*. 101:224–231.e225.
- Eshed, Y., K. Feinberg, S. Poliak, H. Sabanay, O. Sarig-Nadiri, I. Spiegel, J.R. Birmingham Jr., and E. Peles. 2005. Gliomedin mediates Schwann cell-axon interaction and the molecular assembly of the nodes of Ranvier. *Neuron*. 47:215–229. <https://doi.org/10.1016/j.neuron.2005.06.026>
- Ettxeberria, A., K.C. Hokanson, D.Q. Dao, S.R. Mayoral, F. Mei, S.A. Redmond, E.M. Ullian, and J.R. Chan. 2016. Dynamic Modulation of Myelination in Response to Visual Stimuli Alters Optic Nerve Conduction Velocity. *J. Neurosci.* 36:6937–6948. <https://doi.org/10.1523/JNEUROSCI.0908-16.2016>
- Golan, N., E. Kartvelishvily, I. Spiegel, D. Salomon, H. Sabanay, K. Rechav, A. Vainshtein, S. Frechter, G. Maik-Rachline, Y. Eshed-Eisenbach, et al. 2013. Genetic deletion of Cadm4 results in myelin abnormalities resembling Charcot-Marie-Tooth neuropathy. *J. Neurosci.* 33:10950–10961. <https://doi.org/10.1523/JNEUROSCI.0571-13.2013>
- Gollan, L., D. Salomon, J.L. Salzer, and E. Peles. 2003. Caspr regulates the processing of contactin and inhibits its binding to neurofascin. *J. Cell Biol.* 163:1213–1218. <https://doi.org/10.1083/jcb.200309147>
- Lee, S., M.K. Leach, S.A. Redmond, S.Y. Chong, S.H. Mellon, S.J. Tuck, Z.Q. Feng, J.M. Corey, and J.R. Chan. 2012. A culture system to study oligodendrocyte myelination processes using engineered nanofibers. *Nat. Methods*. 9:917–922. <https://doi.org/10.1038/nmeth.2105>
- Li, C., M.B. Tropak, R. Gerlai, S. Clapoff, W. Abramow-Newerly, B. Trapp, A. Peterson, and J. Roder. 1994. Myelination in the absence of myelin-associated glycoprotein. *Nature*. 369:747–750. <https://doi.org/10.1038/369747a0>
- Luong, T.N., H.J. Carlisle, A. Southwell, and P.H. Patterson. 2011. Assessment of motor balance and coordination in mice using the balance beam. *J. Vis. Exp.* (49):2376.



- Marcus, J., J.L. Dupree, and B. Popko. 2002. Myelin-associated glycoprotein and myelin galactolipids stabilize developing axo-glia interactions. *J. Cell Biol.* 156:567–577. <https://doi.org/10.1083/jcb.200111047>
- Maurel, P., S. Einheber, J. Galinska, P. Thaker, I. Lam, M.B. Rubin, S.S. Scherer, Y. Murakami, D.H. Gutmann, and J.L. Salzer. 2007. Nectin-like proteins mediate axon Schwann cell interactions along the internode and are essential for myelination. *J. Cell Biol.* 178:861–874. <https://doi.org/10.1083/jcb.200705132>
- McGonigal, R., J.A. Barrie, D. Yao, M. McLaughlin, M.E. Cunningham, E.G. Rowan, and H.J. Willison. 2019. Glial Sulfatides and Neuronal Complex Gangliosides Are Functionally Interdependent in Maintaining Myelinating Axon Integrity. *J. Neurosci.* 39:63–77. <https://doi.org/10.1523/JNEUROSCI.2095-18.2018>
- McKenzie, I.A., D. Ohayon, H. Li, J.P. de Faria, B. Emery, K. Tohyama, and W.D. Richardson. 2014. Motor skill learning requires active central myelination. *Science.* 346:318–322. <https://doi.org/10.1126/science.1254960>
- Menegoz, M., P. Gaspar, M. Le Bert, T. Galvez, F. Burgaya, C. Palfrey, P. Ezan, F. Arnos, and J.A. Girault. 1997. Paranodin, a glycoprotein of neuronal paranodal membranes. *Neuron.* 19:319–331. [https://doi.org/10.1016/S0896-6273\(00\)80942-3](https://doi.org/10.1016/S0896-6273(00)80942-3)
- Montag, D., K.P. Giese, U. Bartsch, R. Martini, Y. Lang, H. Blüthmann, J. Karthigasan, D.A. Kirschner, E.S. Wintergerst, K.A. Nave, et al. 1994. Mice deficient for the myelin-associated glycoprotein show subtle abnormalities in myelin. *Neuron.* 13:229–246. [https://doi.org/10.1016/0896-6273\(94\)90472-3](https://doi.org/10.1016/0896-6273(94)90472-3)
- Novak, N., V. Bar, H. Sabanay, S. Frechter, M. Jaegle, S.B. Snapper, D. Meijer, and E. Peles. 2011. N-WASP is required for membrane wrapping and myelination by Schwann cells. *J. Cell Biol.* 192:243–250. <https://doi.org/10.1083/jcb.201010013>
- Pan, S., and J.R. Chan. 2017. Regulation and dysregulation of axon infrastructure by myelinating glia. *J. Cell Biol.* 216:3903–3916. <https://doi.org/10.1083/jcb.201702150>
- Park, J., B. Liu, T. Chen, H. Li, X. Hu, J. Gao, Y. Zhu, Q. Zhu, B. Qiang, J. Yuan, et al. 2008. Disruption of Nectin-like 1 cell adhesion molecule leads to delayed axonal myelination in the CNS. *J. Neurosci.* 28:12815–12819. <https://doi.org/10.1523/JNEUROSCI.2665-08.2008>
- Pedraza, L., J.K. Huang, and D. Colman. 2009. Disposition of axonal caspr with respect to glial cell membranes: Implications for the process of myelination. *J. Neurosci. Res.* 87:3480–3491. <https://doi.org/10.1002/jnr.22004>
- Rasband, M.N., and E. Peles. 2015. The Nodes of Ranvier: Molecular Assembly and Maintenance. *Cold Spring Harb. Perspect. Biol.* 8:a020495. <https://doi.org/10.1101/cshperspect.a020495>
- Rios, J.C., C.V. Melendez-Vasquez, S. Einheber, M. Lustig, M. Grumet, J. Hemperly, E. Peles, and J.L. Salzer. 2000. Contactin-associated protein (Caspr) and contactin form a complex that is targeted to the paranodal junctions during myelination. *J. Neurosci.* 20:8354–8364. <https://doi.org/10.1523/JNEUROSCI.20-22-08354.2000>
- Sharma, K., S. Schmitt, C.G. Bergner, S. Tyanova, N. Kannaiyan, N. Manrique-Hoyos, K. Kongi, L. Cantuti, U.K. Hanisch, M.A. Philips, et al. 2015. Cell type- and brain region-resolved mouse brain proteome. *Nat. Neurosci.* 18:1819–1831. <https://doi.org/10.1038/nn.4160>
- Snaidero, N., W. Möbius, T. Czopka, L.H. Hekking, C. Mathisen, D. Verkleij, S. Goebbels, J. Edgar, D. Merkler, D.A. Lyons, et al. 2014. Myelin membrane wrapping of CNS axons by PI(3,4,5)P3-dependent polarized growth at the inner tongue. *Cell.* 156:277–290. <https://doi.org/10.1016/j.cell.2013.11.044>
- Spiegel, I., K. Adamsky, Y. Eshed, R. Milo, H. Sabanay, O. Sarig-Nadir, I. Horresh, S.S. Scherer, M.N. Rasband, and E. Peles. 2007. A central role for Necl4 (SynCAM4) in Schwann cell-axon interaction and myelination. *Nat. Neurosci.* 10:861–869. <https://doi.org/10.1038/nn1915>
- Tait, S., F. Gunn-Moore, J.M. Collinson, J. Huang, C. Lubetzki, L. Pedraza, D.L. Sherman, D.R. Colman, and P.J. Brophy. 2000. An oligodendrocyte cell adhesion molecule at the site of assembly of the paranodal axo-glia junction. *J. Cell Biol.* 150:657–666. <https://doi.org/10.1083/jcb.150.3.657>
- Trapp, B.D., S.B. Andrews, A. Wong, M. O'Connell, and J.W. Griffin. 1989. Colocalization of the myelin-associated glycoprotein and the microfilament components, F-actin and spectrin, in Schwann cells of myelinated nerve fibres. *J. Neurocytol.* 18:47–60. <https://doi.org/10.1007/BF01188423>
- Yang, H.J., A. Vainshtein, G. Maik-Rachline, and E. Peles. 2016. G protein-coupled receptor 37 is a negative regulator of oligodendrocyte differentiation and myelination. *Nat. Commun.* 7:10884. <https://doi.org/10.1038/ncomms10884>
- Zhang, Y., K. Chen, S.A. Sloan, M.L. Bennett, A.R. Scholze, S. O'Keefe, H.P. Phatnani, P. Guarnieri, C. Caneda, N. Ruderisch, et al. 2014. An RNA-sequencing transcriptome and splicing database of glia, neurons, and vascular cells of the cerebral cortex. *J. Neurosci.* 34:11929–11947. <https://doi.org/10.1523/JNEUROSCI.1860-14.2014>
- Zhu, Y., H. Li, K. Li, X. Zhao, T. An, X. Hu, J. Park, H. Huang, Y. Bin, B. Qiang, et al. 2013. Necl-4/SynCAM-4 is expressed in myelinating oligodendrocytes but not required for axonal myelination. *PLoS One.* 8:e64264. <https://doi.org/10.1371/journal.pone.0064264>
- Zonta, B., S. Tait, S. Melrose, H. Anderson, S. Harroch, J. Higginson, D.L. Sherman, and P.J. Brophy. 2008. Glial and neuronal isoforms of Neurofascin have distinct roles in the assembly of nodes of Ranvier in the central nervous system. *J. Cell Biol.* 181:1169–1177. <https://doi.org/10.1083/jcb.200712154>